

Jon Runyon¹

School of Engineering,
Cardiff University,
Cardiff CF24 3AA, UK
e-mail: RunyonJP@cardiff.ac.uk

Anthony Giles

School of Engineering,
Cardiff University,
Cardiff CF24 3AA, UK
e-mail: GilesAP1@cardiff.ac.uk

Richard Marsh

School of Engineering,
Cardiff University,
Cardiff CF24 3AA, UK
e-mail: MarshR@cardiff.ac.uk

Daniel Pugh

School of Engineering,
Cardiff University,
Cardiff CF24 3AA, UK
e-mail: PughDG@cardiff.ac.uk

Burak Goktepe

School of Engineering,
Cardiff University,
Cardiff CF24 3AA, UK
e-mail: GoktepeB@cardiff.ac.uk

Philip Bowen

School of Engineering,
Cardiff University,
Cardiff CF24 3AA, UK
e-mail: BowenPJ@cardiff.ac.uk

Steve Morris

School of Engineering,
Cardiff University,
Cardiff CF24 3AA, UK
e-mail: MorrisSM@cardiff.ac.uk

Characterization of Additive Layer Manufacturing Swirl Burner Surface Roughness and Its Effects on Flame Stability Using High-Speed Diagnostics

In this study, two Inconel 625 swirl nozzle inserts with identical bulk geometry were constructed via additive layer manufacturing (ALM) for use in a generic gas turbine swirl burner. Further postprocessing by grit blasting of one swirl nozzle insert results in a quantifiable change to the surface roughness characteristics when compared with the unprocessed ALM swirl nozzle insert or a third nozzle insert which has been manufactured using traditional machining methods. An evaluation of the influence of variable surface roughness effects from these swirl nozzle inserts is therefore performed under preheated isothermal and combustion conditions for premixed methane-air flames at thermal power of 25 kW. High-speed velocimetry at the swirler exit under isothermal conditions gives evidence of the change in near-wall boundary layer thickness and turbulent fluctuations resulting from the change in nozzle surface roughness. Under atmospheric combustion conditions, this influence is further quantified using a combination of dynamic pressure, high-speed OH chemiluminescence, and exhaust gas emissions measurements to evaluate the flame stabilization mechanisms at the lean blowoff and rich stability limits. Notable differences in flame stabilization are evident as the surface roughness is varied, and changes in rich stability limit were investigated in relation to changes in the near-wall turbulence intensity. Results show that precise control of in-process or postprocess surface roughness of wetted surfaces can positively influence burner stability limits and NO_x emissions and must, therefore, be carefully considered in the ALM burner design process as well as computational fluid dynamics (CFD) models. [DOI: 10.1115/1.4044950]*

1 Introduction

For over two decades, additive layer manufacturing (ALM), also known as additive manufacturing or 3D printing, has been developed as a breakthrough enabler of novel component design and fabrication, offering reduced costs, improved logistics, and positive sustainability impact when compared with traditional machining methods [1,2]. The technology has also been shown to significantly reduce product development cycles through rapid and iterative prototyping [3]. Metallic ALM has recently emerged as a commercial technology for the production of gas turbine parts given the potential for significant performance improvements using complex geometries, light-weighting, and multiple component integration [4,5]. Industrial and micro gas turbine manufacturers such as General Electric (Boston, MA) [6], Siemens (Munich, Germany) [7,8], Mitsubishi Heavy Industries (Tokyo, Japan) [9], Solar Turbines (San Diego, CA) [10], MAN Diesel and Turbo (Augsburg, Germany) [11], and Capstone Turbine Corporation (Van Nuys, CA) [12] are investing in and researching the use of ALM for the production of new components and also for

the repair of in-service equipment, including burners [13]. Critical gas turbine parts such as fuel nozzles [6], turbine blades [7], burners [8], and guide vanes [11] are now in commercial production and, in some cases, have extended in-service lifetimes [13].

Of particular interest to this work, gas turbine burner swirlers are considered a prime candidate for fabrication and design enhancement using metallic ALM [7,14], with flame stabilization, fuel flexibility, pressure drop, and fuel/air mixing the key parameters for improvement. Giuliani et al. [14] fabricated three Inconel 718 axial swirl generators using powder and a selective laser melting (SLM) process in a Farsoon FS121M machine. These axial swirlers used a novel single vane S-shape design that improved the lean blow off (LBO) behavior while reducing the pressure drop when compared with a similar typical axial swirler of heli-coid (X-shape) design [14]. It was noted that the surface roughness of the unfinished, “raw,” ALM swirlers has a measureable influence on the pressure drop, with build orientation and angle relative to the x - y plane both highlighted as significant factors [14]. However, no further postprocessing of the surface or detailed study into the direct effect of surface roughness on the swirl flow and flame stabilization was conducted in that study.

Surface roughness of metallic ALM components and subsequent postprocessing are considered key areas of research need.

¹Corresponding author.

Manuscript received July 1, 2019; final manuscript received July 13, 2019; published online February 4, 2020. Editor: Jerzy T. Sawicki.

This includes topics such as how to control this feature during the build process and the potential to integrate advantageous surface finishes into the build [1,12,15]. For many years, the influence of surface roughness on flow has been a focal point, including fundamental studies which directly highlight aspects critical to swirl-stabilized combustion. Achenbach and Heinecke [16] observed that increasing surface roughness can influence vortex shedding and drag coefficient from a cylinder in cross-flow in addition to reducing the boundary layer separation angle when compared with a smooth cylinder [16]. Surface roughness has also been shown to increase the wall shear stress, resulting in reduced Reynolds stress anisotropy related to wall-normal velocity fluctuations particularly in the inner region of the boundary layer [17]. Increasing surface roughness peak density and peak shape have also been shown to enhance wall heat transfer in microchannels, indicated in a CFD modeling study by a reduction in Nusselt number [18].

A limited number of studies have focused on the effect of surface roughness on specific combustion phenomena. Maeda et al. [19] utilized time-sequential Schlieren imaging to detail the influence of surface roughness on the deflagration-to-detonation transition of H_2-O_2 mixtures in a 12 mm \times 10 mm channel, noting that the roughness increased flame acceleration, reducing the time of transition to detonation when compared with a smooth wall. In swirl combustion, Al-Fahham et al. [20] considered the use of biomimetic microspheres in a burner nozzle to enhance boundary layer flashback resistance, observing a reduction in the thickness of the near-wall velocity gradient, a reduction in boundary layer turbulence intensity, and a positive shift in the flashback equivalence ratio, ϕ . Finally, Pritz et al. [21] found improved agreement between experimental results and large eddy simulation which included surface roughness along selected geometric boundaries versus smooth walls, confirming that surface roughness can influence flow and flame stability. Thus, with the recent emergence of ALM as a tool for gas turbine combustor components, the need for and cost of postprocessing the components, and the potential for novel surface finishes, the impact of surface roughness on combustion systems requires further systematic study.

1.1 Investigation Aim. In this study, the influence of ALM surface roughness and postbuild surface finishing is analyzed in the context of a radial-tangential gas turbine swirler. This swirler, a version of which has been manufactured by traditional machining methods, is part of the second generation high-pressure generic swirl burner (HPGSB-2) and is well-characterized in terms of its stable operating limits (e.g., LBO and flashback), fuel flexibility, and emissions [22–24]. By comparing this “traditional” swirler with two ALM swirlers, one “raw” and the other postprocessed using a grit blast to reduce the surface roughness, this study aimed to identify and evaluate the influence of varying surface roughness on the resulting swirl flow boundary layers and turbulence, flame stability limits, and emissions. This is accomplished through the use of high-speed, time-resolved velocimetry, OH^* chemiluminescence, and dynamic pressure measurements. All three swirlers have the same bulk geometric features, yielding a geometric swirl number of $S_g = 0.8$.

The results of this study aimed to provide a detailed experimental basis for the consideration of ALM surface roughness and potential postprocessing during the design phase of critical flow-developing gas turbine combustion components. This includes addressing surface roughness in CFD analysis, which has been identified as a topic worthy of considerable attention in gas turbines [25]. This study will inform further work with novel swirler geometries and the development of advantageous, engineered ALM surface features, which are suggested to become commonplace in future gas turbines [25].

2 Experimental and Diagnostic Setup

2.1 Swirler Design and Operating Conditions. Isothermal air flow and preheated atmospheric pressure ($P_2 = 0.110$ MPa)

combustion experiments up to 573 ± 5 K inlet temperature (T_2) were conducted in Cardiff University Gas Turbine Research Centre’s high-pressure combustion rig, which includes a variable speed drive air compressor, air dryer, two electric air preheaters in series, the high-pressure optical chamber (HPOC) housing the experimental swirl burner, and a backpressure valve for rig pressurization. When installed in the HPOC, the HPGSB-2 allows optical access to the flame through the use of quartz windows and a cylindrical quartz burner confinement with 100 mm inner diameter and 385 mm in length. Further information regarding this experimental rig and the design of the HPGSB-2, shown in Fig. 1, can be found in other works by the authors [22–24]. A bluff-body instrumentation lance with 18 mm OD is placed down the centerline of the HPGSB-2 and allows for temperature measurement (K-type, ± 2.2 K) within the burner exit nozzle. The HPGSB-2 is modular in that it can be operated with a variety of swirl numbers and confinements, with previous studies including low swirl numbers of $S_g = 0.5$ and novel convergent quartz confinements [26]. For this study, S_g was held constant at 0.8.

The swirlers utilized in this study include a “raw” ALM swirler (no postbuild surface finishing) with $S_g = 0.8$ (“8R”, Fig. 2(a)), a grit blasted ALM swirler with $S_g = 0.8$, (“8G”, Fig. 2(b)), a machined swirler with $S_g = 0.8$ (“8M”, Fig. 2(c)). Critical dimensions (e.g., nozzle radius) and the location of laser Doppler anemometry (LDA) measurements are also given in Fig. 2. The 304 stainless steel 8M swirler was fabricated at Cardiff University and has been utilized previously for preheated, pressurized combustion studies [22–26]. The ALM swirlers were manufactured by HiETA Technologies Limited in Bristol, England using a Renishaw RenAM 500Q powder bed SLM machine, which utilizes four 500 W lasers, an argon inert atmosphere, and a 250 mm \times 250 mm \times 350 mm build volume. The powder used for construction was Inconel 625 (LPW Technology Ltd), selected due to its high-strength characteristics at elevated temperature, and which has been used in other studies of SLM construction with regard to surface roughness [15]. Both swirlers were collocated on the build plate along with 6 mm diameter tensile bars and a density block for postbuild quality assurance. A postbuild heat treatment was utilized to eliminate residual stresses induced during the build. Support structures were removed from all surfaces of the swirlers, however, only the 8G swirler was then postprocessed using a manual grit blast (Guyson Saftigrit Brown 24, Rolls Royce CSS12 standard) and bead (Guyson Turbonox) application to improve the swirler surface finish, visible in Fig. 2(b).

All combustion studies were conducted under lean ($0.50 < \phi < 0.95$) conditions, with fully premixed methane-air at a fixed thermal power of 25 kW. The fuel flow rate was fixed to maintain the power density scaling (250 kW/MPa [23]) required for future pressurized combustion experiments. The stable operating limits for each of the three swirlers were obtained by varying the equivalence ratio from LBO to a noted rich stability event or $\phi = 0.95$,

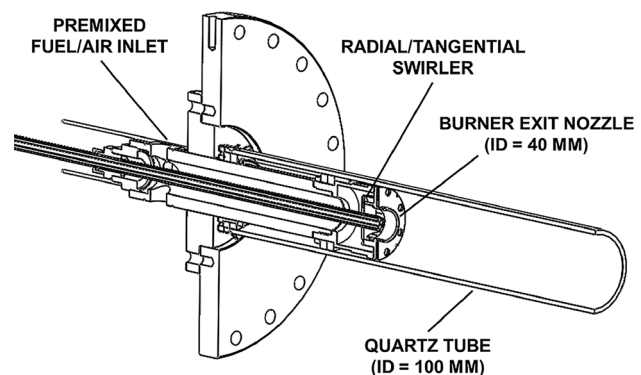


Fig. 1 Cut-away schematic of HPGSB-2 with $S_g = 0.8$ radial/tangential swirler installed (flow from left to right)

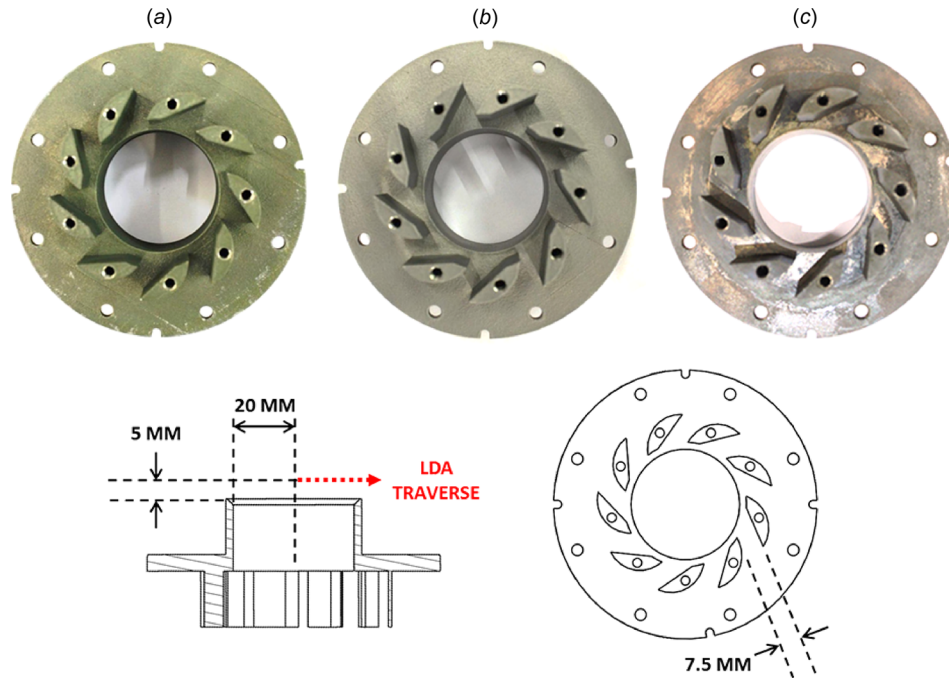


Fig. 2 ALM swirler vanes, (a) 8R, (b) 8G, and (c) 8M with cross section, geometry, and LDA measurement location

whichever occurred first. The burner was ignited at a stable operating condition and ϕ was reduced toward LBO by increasing the air mass flow rate and then increased toward stoichiometry by reducing the air mass flow rate. LBO was categorized by abrupt flame transition into a low-frequency, high-amplitude limit cycle instability characterized by macro flame extinction and reignition events, which have been documented previously in this burner with $S_g = 0.8$ under ambient inlet conditions [22]. The rich stability limit was characterized by one of two events, an abrupt change in the dynamic pressure amplitude into a limit cycle as ϕ was increased (as seen with swirler 8R) or $\phi = 0.95$ (as seen with swirlers 8G and 8M), at which high NO_x and CO emissions would make operation unfeasible.

With a fixed CH_4 flow rate of 0.5 g/s, the range of air flows achieved in this study were 9.08–17.14 g/s. This yields a Reynolds number range of approximately 10,500–19,100 and mean nozzle exit axial velocities, \bar{u} , of 11.9–21.6 m/s, both based on premixed reactant volumetric flow through the 40 mm ID burner exit nozzle. For LDA measurements, isothermal air flows were utilized, ensuring that temperature, pressure, total mass flow, and Reynolds number at the burner exit ($\pm 3\%$) were maintained with the equivalent combustion conditions. The air and fuel flows were measured by Micro Motion ELITE coriolis mass flow meters allowing for flow accuracies of $\pm 0.5\%$. Premixed burner inlet temperature (T_2) and pressure (P_2) were measured at the location indicated in Fig. 1 by a K -type thermocouple (± 2.2 K) and a Druck PDCR 10/T pressure transducer ($\pm 0.04\%$), respectively. Burner outlet temperature (T_3 , N -type, ± 1.1 K) was measured at the exit of the quartz cylinder. A dedicated swirler pressure drop measurement, ΔP , was made with a Druck PDCR 10/35 L differential pressure transducer ($\pm 0.04\%$ full scale to 70 kPa). Finally, dynamic pressure measurements at the burner dump plane were sampled at 4000 Hz with a PCB 113B28 piezoelectric dynamic pressure transducer with 14.5 mV/kPa sensitivity ($\pm 15\%$) and 0–350 kPa range, with postprocessing conducted via fast Fourier transform to identify pressure fluctuation amplitude, p_{RMS} , as well as dominant and secondary mode frequencies, f_1 and f_2 , and their individual amplitudes, M_{f_1} and M_{f_2} . All other rig operating conditions (e.g., flows, temperatures, pressures) were logged at 1 Hz by a dedicated data acquisition system.

2.2 Experimental Diagnostics

2.2.1 High-Speed OH^* Chemiluminescence.

The high-speed OH^* chemiluminescence image capture system, shown in Fig. 3 assembled for measurement through a side window of the HPOC at 90 deg to the HPGSB-2, utilizes a combination of high-speed camera, relay lens, high-speed image intensifier, UV lens (Ricoh FL-GC7838-VGUV, $f/16$), and 310 nm narrow bandpass filter. The high-speed camera is a monochromatic Vision Research Phantom v1212 with 72 Gb on-board memory and up to 12,000 frames/second at full resolution (1280×800) and bit depth of 12 bits. The image intensifier is a specialized imaging limited SIL40HG50 with UV-enhanced S20 photocathode and maximum frame rate of 100,000 frames/s. For this study, the system was operated at 4000 Hz, with the exposure time of the image intensifier set at 10 μs and the gain held constant across all conditions. The system is remotely triggered and controlled by a dedicated computer system using vision research PCC 2.8 and specialized imaging limited SILCONTROL2 software. A target image was utilized to provide the resolution, equal to 4.75 pixels/mm. The camera resolution was down-selected to reduce file size to 768×576 pixels, resulting in a field of view of 162 mm (axial, y) \times 121 mm

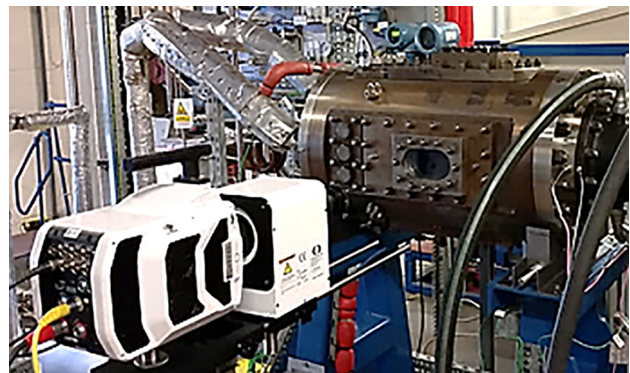


Fig. 3 Photograph of high-speed OH^* chemiluminescence system with HPOC and HPGSB-2 installed (flow from left to right)

(radial, r) relative to the edge and centerline of the burner exit nozzle, respectively.

For averaged images presented in this study, each instantaneous OH* chemiluminescence image was filtered using a 3×3 pixel median filter and corrected for background intensity before being temporally averaged from 2000 images ($t = 0.5$ s). The temporally averaged images were then processed using a modified Abel inversion algorithm to provide an axisymmetric planar representation of the localized areas of heat release within the field of view [22]. For phase-averaged images, the number of images used is directly proportional to the number of phases presented and the period of the dominant instability frequency, and will be noted in each figure. Temporal variation of the OH* chemiluminescence signal is also considered through the use of an instantaneous integral intensity, Π'_{OH^*} [22].

2.2.2 High-Speed Velocimetry. A 1D Dantec Dynamics flow-lite LDA system was used for characterizing the influence of surface roughness on the mean flow field and turbulence characteristics of isothermal air flow conditions in each swirler. Two flow conditions were selected, equivalent to the $\phi = 0.55$ and $\phi = 0.80$ conditions, with mean nozzle exit axial velocities of $\bar{u} = 20.7$ m/s and 14.5 m/s, respectively. This maintains Reynolds number ($\pm 3\%$) with the equivalent $\phi = 0.55$ and $\phi = 0.80$ conditions, with $Re = \sim 17,500$ and $\sim 12,000$, respectively. This backscatter system utilizes a 200 mW constant wave Nd:YAG laser (532 nm) split to produce two beams, one of which is frequency shifted by a Bragg cell operating at 40 MHz. Fiber optics carry the beams to a combined transmitting/receiver optic (beam separation 38 mm, focal length 500 mm) together with the detected signal produced by particles traversing the control volume. The air flow was seeded with $1 \mu\text{m}$ nominal diameter Al_2O_3 . The burst signal was processed using a BSA F60 processor and Dantec BSA FLOW software to yield the mean and RMS velocities at the control volume location. In this study, the mean and fluctuating axial velocity components, u and u'_{RMS} , were measured 5 mm downstream of the burner exit nozzle as shown in Fig. 2. The transmitting and receiving optics were mounted on a traverse system which allowed the control volume to be maneuvered throughout the flow field. Starting from the burner centerline ($r = 0$ mm), the control volume was moved radially to a final position outside the burner exit nozzle ($r = 30$ mm), refer to Fig. 2. Measurements were taken at 1 mm increments for the first 15 mm and last 5 mm covered, with 0.5 mm increments used for the area either side of the burner nozzle ID wall ($15 \text{ mm} < \text{ID wall} < 25 \text{ mm}$), for a total of 41 measurements. To investigate the near-wall velocity and turbulence intensity at the burner exit, the isothermal flow measurements were conducted with the quartz confinement removed from the HPGSB-2. Data capture rates up to 40,000 points or 25 s of capture time were achieved by controlling the seeding rate and density.

2.2.3 Exhaust Gas Analysis. Exhaust gas sampling and analysis was conducted via an industry standard system supplied by Signal Gas Analysers Ltd. An equal area sample probe was placed 200 mm downstream of the exit of the cylindrical quartz confinement. The exhaust gas sample line, filter, and distribution manifolds were maintained at 433 K, while a heated pump was used to draw sample into the analyzer setup. Total NO_x concentrations were measured using a heated vacuum chemiluminescence analyzer (Signal Instruments 4000VM), calibrated in the range of 0–39 ppmV. Total NO_x concentrations were measured hot and wet to avoid any losses, with data presented at the equivalent dry conditions using a calculated equilibrium water molar fraction, $X_{\text{H}_2\text{O}}$, and adiabatic flame temperature (AFT) from CHEMKIN [27] using GRI-Mech 3.0 [28]. NO_x emissions were then normalized to a reference value of 15% O_2 concentration per Eqs. (1) and (2), respectively. Exhaust molar O_2 measurements were made using a paramagnetic analyzer (Signal Instruments 9000MGA), calibrated in the range 0–22.52 vol % O_2 . Typical uncertainties of approximately 5% of measurement account for analyzer specifications, linearization, and accuracy in span gas certification

$$\text{NO}_x, \text{ dry} = \frac{\text{NO}_x, \text{ meas}}{(1 - X_{\text{H}_2\text{O}})} \quad (1)$$

$$\text{NO}_x, \text{ dry, 15\% O}_2 = \text{NO}_x, \text{ dry} * \left(\frac{20.9 - \text{O}_2, \text{ ref}}{20.9 - \text{O}_2, \text{ meas}} \right) \quad (2)$$

2.2.4 Surface Roughness Measurements. The form and surface roughness of five separate surfaces on each of the two ALM swirlers (8R and 8G) as well as the machined swirler (8M) were conducted using a Taylor Hobson Form TalySurf Series 2 profilometer, used extensively for tribology and SLM surface roughness studies [29,30]. A standard inductive pick-up stylus arm with a 90 deg conisphere diamond styli with $2 \mu\text{m}$ nominal radius was used with a 16 nm vertical resolution. This inductive gauge is calibrated over a 12.5 mm radius. As far as reasonably practicable, measurements and the corresponding surface roughness analysis were performed per the guidelines given in BS EN ISO 4287/4288. For example, the upper and lower cut-off lengths for the ALM components were 2.5 mm and 0.0025 mm, respectively, due to anticipated mean surface roughness, R_a , values greater than $2 \mu\text{m}$. The upper and lower cut-off lengths for the machined swirler were 0.8 mm and 0.0025 mm, respectively. For each swirler, five separate surfaces were characterized as follows (and shown in Fig. 4):

- (1) *Nozzle ID* (“ID”). The inner diameter of the 40 mm swirler exit nozzle was measured at nine locations, thus 40 deg intervals, in the direction from the swirler base plate to the edge of the nozzle (also the direction of air/fuel flow). The measurement length was 20 mm. This surface is parallel to the ALM build direction.
- (2) *Swirl base* (“SB”). Each swirler consists of nine swirl vanes which stand perpendicular to a flat base plate. Between each swirler, this base was measured from near the exit nozzle ID to the OD of the swirler base plate. The measurement length was 20 mm. This surface is perpendicular to the build direction.
- (3) *Swirl curve* (“SC”). On the center of each swirl vane, the curved surface of the swirl vane was measured along the radius, providing a measure of the radius and the surface roughness. The measurement length was 7 mm, limited by the range of the inductive gauge. This surface is perpendicular to the build direction.
- (4) *Swirl curve length* (“SCL”). On the center of each swirl vane, the length of the curved surface was measured in the direction from the base plate to the top of the swirl vane. The measurement length was 10 mm, limited by the length of the swirl vane perpendicular to the swirl base plate. This surface is parallel to the build direction.
- (5) *Swirl flat length* (“SFL”). The flat on the trailing edge of the swirl vane surface was measured in the direction from the base plate to the top of the swirl vane. The measurement length was 10 mm. This surface is parallel to the build direction.

3 Results and Discussion

3.1 Surface Finish and Critical Form Variation. Prior to conducting isothermal and combustion experiments, surface roughness and profile measurements were made on each swirler. Note however that the 8M swirler was in a “used” condition. Table 1 provides commonly cited surface roughness parameters for each swirler from each surface detailed above: R_a (arithmetic average surface roughness), R_q (RMS surface roughness), and R_z (ten-point average surface roughness as a measure of five highest peaks and five lowest valleys). The average overall R_a value for the “raw” ALM swirler, 8R, is approximately $8.5 \mu\text{m}$, if the swirler base is neglected due to its distinctly different finish. The

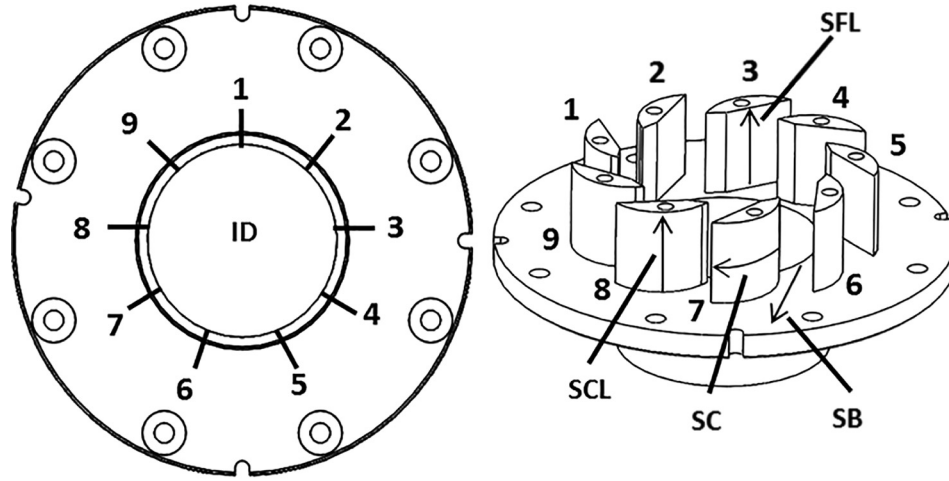


Fig. 4 Surface roughness measurement locations of ALM and machined swirlers

swirler base shows higher surface roughness across both ALM components, as the result of partially bonded powder particles on the surface perpendicular to the build direction, which does not undergo any further laser sintering during the build-up of the swirl vanes [30]. Each swirler was subjected to further sintering as each was built up from the base, resulting in an improved finish on its outer surfaces, including along the swirler curve direction, resulting in a difference in surface finish between the swirler base and swirler curve despite both being perpendicular to the build direction. These values of R_a are similar to those seen in the literature for “raw” unfinished ALM components [30].

In addition, a “raw” swirler with $S_g = 2.0$, which is the subject of future study, was also included on the same build plate as the 8R and 8G swirlers. The same surface roughness measurements were also conducted with this additional swirler to quantify part-to-part variation in “raw” R_a values. If the SB surface is neglected as previously described, the average deviation in R_a values was $\pm 0.2 \mu\text{m}$ between the raw 8R and $S_g = 2.0$ swirlers, with some surfaces R_a values (e.g., ID and SFL) deviating by only $\pm 0.06 \mu\text{m}$. This confirms a consistent “raw” surface finish was generated between components on the build plate. The grit-blasted swirler, 8G, shows a reduction in all surface roughness values of approximately 40% compared to the unfinished ALM component, impacted mostly by a reduction in surface peak values. The traditionally machined swirler, 8M, was found to have R_a values of approximately 15% of that for the “raw” swirler, 8R, and approximately 25% of that for the grit-blasted swirler, 8G.

In addition to the surface roughness measurement, a measure of the swirler radius was also made along the “SC” surface, a critical flow-developing surface. The nominal design value of this radius is 12 mm for all swirlers. The ALM swirl vanes were found to better replicate this curved profile than the machined swirl vanes, with an average value of 11.971 mm compared to 11.864 mm,

respectively. These dimensional deviations fall within BS EN 20286 standard tolerance grades, IT9 for the ALM swirlers and IT12 for the machined swirler. This is in agreement with expected tolerance class limits for ALM and milling processes in the literature [31]. Further manufacturing tolerance evaluation of the raw ALM swirlers (8R and 8G prior to grit-blasting) was also conducted using a GOM 3D coordinate measuring system, with average deviations from design values falling within $\pm 0.100 \text{ mm}$, again in agreement with values in the literature [31]. A radial profile measurement of the swirl vane, showing increased surface roughness of the ALM swirlers, is given in Fig. 5.

3.2 Swirl Flow Characterization. Turbulent swirling flows exhibit complex fluid dynamics phenomena that require temporally and spatially resolved measurements in order to characterize unique structures, such as the central recirculation zone (CRZ) or turbulent shear layer, that are developed as a result of pressure and velocity gradients in the flow field. Previous measurements to identify these structures in the HPGSB-2 have relied on low-speed (5 Hz) particle image velocimetry measurements [22]. LDA is one such measurement that provides simultaneous temporal and spatial measurements of both mean and fluctuating axial velocity components, with spatial resolution dictated by the laser control volume size and traverse increments. By combining the mean and fluctuating axial velocity components, u and u'_{RMS} , it is possible to obtain a measure of the turbulence intensity as given in the following equation:

$$\text{turbulence (\%)} = 100 * \left(\frac{u'_{\text{RMS}}}{u} \right) \quad (3)$$

The values used in Eq. (3) were weighted by the transit time of seed particles through the control volume, so as not to bias regions

Table 1 Average surface roughness measurements for each generic swirler

Swirler	Measurement	Measurement location (or \perp , relative to ALM build direction)				
		Nozzle ID ()	Swirler base (\perp)	Swirler curve (\perp)	Swirler curve length ()	Swirler flat length ()
8R	R_a (μm)	8.88	11.09	8.31	8.31	8.59
	R_q (μm)	10.97	14.92	10.29	10.14	10.64
	R_z (μm)	53.61	78.11	50.01	47.91	54.06
8G	R_a (μm)	5.48	8.12	5.13	4.73	4.92
	R_q (μm)	6.96	10.36	6.36	6.05	6.21
	R_z (μm)	35.50	49.57	31.15	31.06	33.54
8M	R_a (μm)	1.39	1.76	0.67	0.97	1.26
	R_q (μm)	1.88	3.31	1.04	1.24	1.75
	R_z (μm)	8.96	11.21	4.27	6.12	9.07

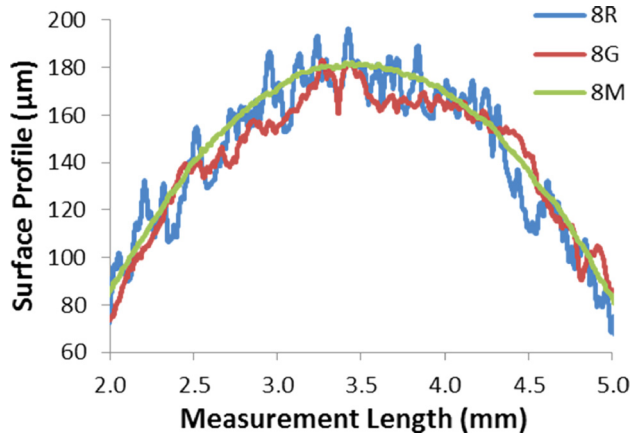


Fig. 5 Surface profile and roughness measurement of swirl vane radius

of high velocity which would be expected to have higher seeding densities. Axial velocity and turbulence intensity profiles measured 5 mm above the burner exit are given in Figs. 6 and 7. Two isothermal air flow conditions were investigated, with equivalent total mass flow to $\phi = 0.55$ (Figs. 6(a) and 7(a)) and 0.80 (Figs. 6(b) and 7(b)) combustion conditions, yielding bulk mean axial velocities of $\bar{u} = 20.7$ m/s and 14.5 m/s, respectively. Figure 6 details the axial velocity component along the radial direction, providing indication of the flow structures mentioned previously, with a CRZ identified by negative magnitude velocities from $0 < r < \sim 10$ mm, a shear layer with $u = 0$ m/s velocity, positive outward flow from ~ 10 mm $< r < 30$ mm and an outer recirculation zone causing reduced velocities after the swirl nozzle ID wall located at $r = 20$ mm. At both flow rates, the maximum positive axial velocity is seen to reduce with increasing surface roughness. For example, in Fig. 6(a), maximum positive axial velocity decreases by 6.6% from 28.2 m/s (8M) to 26.3 m/s (8R) for the same volumetric flow. This is due to an increase in the pressure drop across the swirler with increasing surface roughness, with ΔP increasing from 0.96 kPa (8M) to 1.11 kPa (8R) for the $\phi = 0.55$ flow condition. An increase in the CRZ strength is also

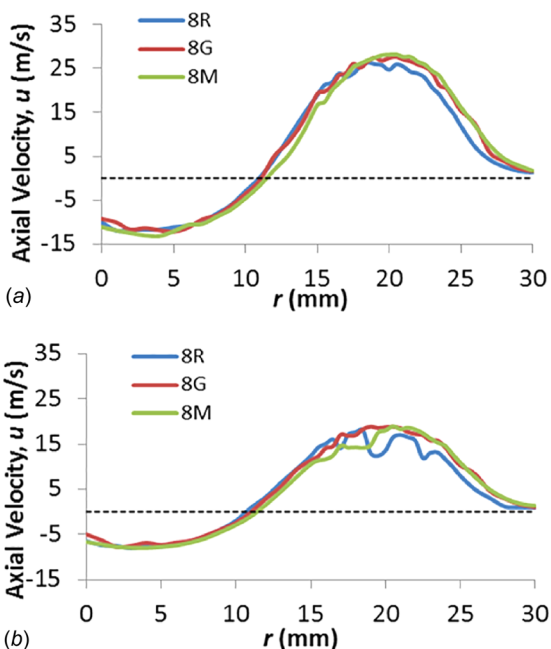


Fig. 6 Axial velocity profiles at equivalent air flow to (a) $\phi = 0.55$ and (b) 0.80. Zero axial velocity shown as dashed line.

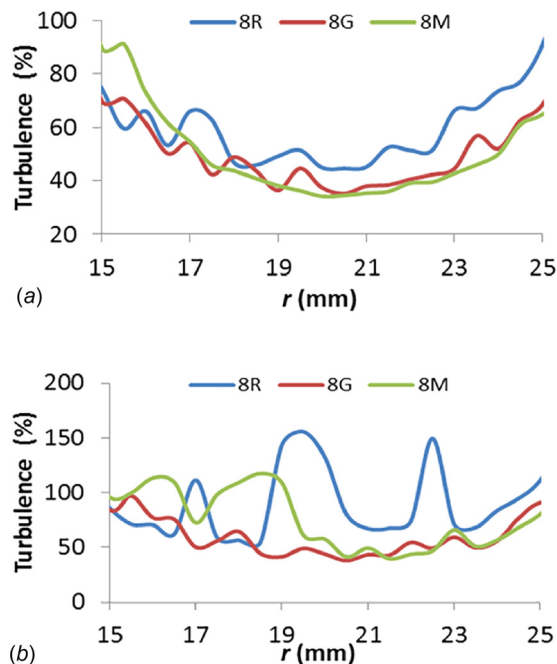


Fig. 7 Turbulence intensity profiles at equivalent air flow to (a) $\phi = 0.55$ and (b) 0.80. Note change in y-axis scale.

noted, with higher magnitude negative axial velocities for the 8M swirler compared with the ALM swirlers. This corresponds to the observed outward radial shift of the velocity peak with reduced surface roughness.

The velocity profiles are notably more variable at the reduced flow rates (Fig. 6(b)), influenced by higher turbulence fluctuations, as shown in Fig. 7(b), particularly near the nozzle ID wall at $r = 20$ mm. At the high-flow conditions (Fig. 7(a)), the turbulence intensity near the nozzle ID wall is shown to increase with increasing surface roughness. At the low-flow condition (Fig. 7(b)), the results are more variable with particularly interesting response from the 8R swirler at $\phi = 0.80$ conditions (Fig. 7(b)). The reduction in axial velocity magnitude near the nozzle ID wall and corresponding increase in turbulence intensity suggests increased vortex formation in this region, interpreted by the LDA system as contributing a negative axial velocity component to the flow. This increasing turbulence intensity serves to spread the region of maximum velocity gradient seen in the profiles in Fig. 6. By fitting a high-order polynomial function to the velocity profiles in Fig. 6 and evaluating its first derivative to locate maxima and minima on either side of the peak positive axial velocity position, the width of the maximum velocity gradient could be evaluated. The width of this region increases by 9.6% from 8M to 8R (11.5–12.6 mm) at $\phi = 0.55$ conditions and by 14.6% from 8M to 8R (12.6–14.5 mm) at $\phi = 0.80$ conditions; a similar response which has been observed by others and corresponds to a reduced boundary layer thickness at the burner exit nozzle with increasing surface roughness of the nozzle ID wall [20].

3.3 Swirl Flame Behavior and Stability

3.3.1 Flame Location. With an understanding of the influence of surface roughness on the flow field, combustion experiments were conducted at fixed thermal power of 25 kW and a range of equivalence ratios to evaluate the influence of varying surface roughness on the flame location and stable operating range. While a wide operating range was investigated, the results presented herein focus first on the same flow conditions as presented in the isothermal velocimetry measurements in Sec. 3.2, namely, $\phi = 0.55$ and 0.80. Figure 8 provides Abel-transformed OH* chemiluminescence images for these two equivalence ratios along

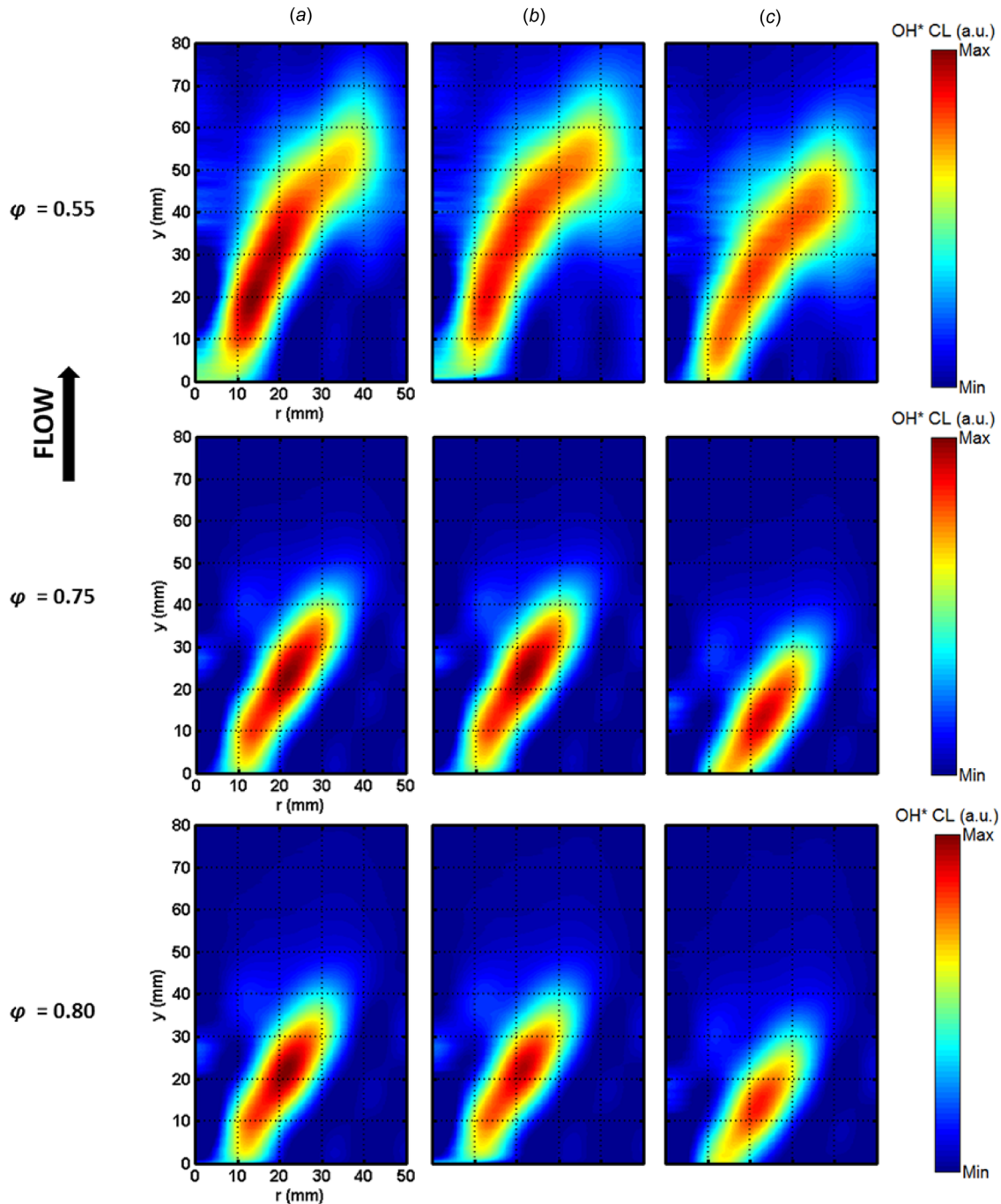


Fig. 8 Abel transformed OH* chemiluminescence images for (a) 8R, (b) 8G, and (c) 8M at $\phi = 0.55$, $\phi = 0.75$, and $\phi = 0.80$. Colormap normalized to maximum OH* intensity at each ϕ .

with $\phi = 0.75$ for swirlers 8R (Fig. 8(a)), 8G (Fig. 8(b)), and 8M (Fig. 8(c)). The field of view expands axially downstream from the burner exit nozzle ($y = 0$ mm) and radially outward from the burner centerline ($r = 0$ mm). Images for each fixed ϕ are presented with a false colormap normalized to the maximum OH* intensity value in each set. Each swirler generates a V-shape flame which has been observed previously for this burner at atmospheric temperature inlet conditions [22].

This is to be expected as the flame lies on the outward expanding shear layer of near-zero axial velocity between the CRZ and the outward positive flow. The flame is also observed to transition toward the burner exit nozzle along the shear layer as ϕ is increased, resulting from a combination of reduced axial velocity and increased burning rate. For the $\phi = 0.55$ condition, the area of

increased heat release is observed to initiate at a location ($r = 10$ mm, $y = 5$ mm) similar to that identified as the shear layer in the corresponding isothermal flows (Fig. 6(a)), with the shear layer (and flame) shifting radially outward with a reduction in surface roughness. A similar response can be seen for the $\phi = 0.75$ and $\phi = 0.80$ conditions. This suggests that in addition to influencing the axial velocity component, the surface roughness may also have an effect on the tangential velocity component (thus, local swirl number) at the burner exit nozzle and will be the subject of further study.

Also of interest is the change in OH* chemiluminescence intensity and location of maximum intensity. For both $\phi = 0.55$ and $\phi = 0.80$, the maximum OH* intensity is measured in the 8R swirler flame, and decreases with decreasing surface roughness. This

is attributed to enhanced heat release along the shear layer induced by the increased turbulence intensity noted in Fig. 7, which acts to increase localized flame consumption speed [32]. At $\phi=0.75$, the maximum OH^* intensity is nominally constant between the 8R and 8G swirlers, with the 8G swirler shown to exhibit bimodal stability at this condition, discussed in Sec. 3.3.2. However, this is only a localized effect as the exhaust temperatures for all three swirlers are $T_3=1204 \pm 6$ K, 1270 ± 5 K, and 1282 ± 4 K for $\phi=0.55$, $\phi=0.75$, and $\phi=0.80$, respectively. As the swirler surface roughness is decreased (left to right for fixed ϕ in Fig. 8), the flame is observed to transition axially upstream and radially outward. This is in agreement with the change in the velocity profiles for the similar isothermal flow conditions presented in Fig. 6 and is further confirmed by the plot in Fig. 9 of the OH^* chemiluminescence intensity centroid location, calculated using the procedure described in Ref. [33]. Figure 9 provides a measure of the movement of the heat release zone with change in surface roughness and burner operating conditions from $\phi=0.55$ (closed symbols) to $\phi=0.75$ (hatched symbols) to $\phi=0.80$ (open symbols). An increase in flame angle relative to the burner centerline is also quantified for a reduction in surface roughness, particularly at $\phi=0.55$. It is also worthy of note that as the surface roughness increases, the flame stabilization location shifts toward the radial position of the nozzle ID wall at $r=20$ mm, indicative of the increased influence that this feature imparts on the flow field.

3.3.2 Flame Stability. The dynamic behavior of the 25 kW flame with varying swirler surface roughness was also considered across the entire operating range using high-speed dynamic pressure and OH^* chemiluminescence. A measure of the dynamic response of the system is given in Fig. 10, which plots the dynamic pressure amplitude, p'_{RMS} (Fig. 10(a)) and dominant mode frequency, f_1 (Fig. 10(b)), against equivalence ratio. In general, the operating range is bounded by limits marked by LBO at approximately $\phi=0.50$ and a rich operating limit, either $\phi=0.81$ (8R) or $\phi=0.95$ (8G and 8M). The 8M swirler has distinct stable operating regimes between $0.50 < \phi < 0.60$ and $0.65 < \phi < 0.90$. Increasing the surface roughness from 8M to 8R is shown to reduce the instability amplitude observed at $\phi=0.60$. However, increased surface roughness in the 8R swirler introduces a potential thermoacoustic instability at $\phi=0.81$ at approximately 400 Hz. This is also suggested in Fig. 11(a), where the secondary mode frequency, f_2 , is observed to be equal to $2f_1$ (i.e., second harmonic) for the 8R swirler at $\phi=0.81$ (note the value of f_2 is off-scale in this plot). This is attributed to the unique near-wall turbulence profile seen for the 8R swirler at near identical flow conditions in Fig. 7(b), which would serve to

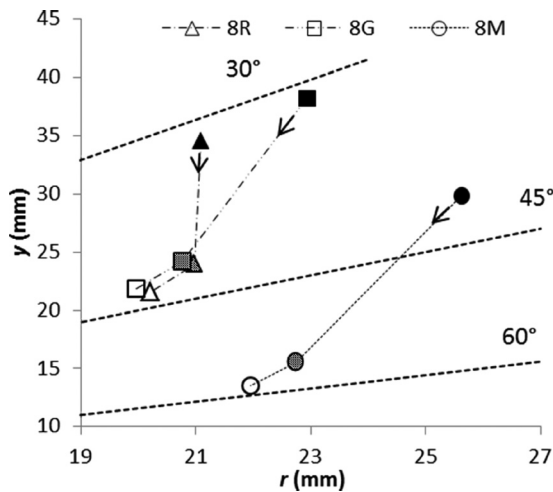


Fig. 9 OH^* centroid location movement from $\phi=0.55$ (closed) to $\phi=0.75$ (hatched) to $\phi=0.80$ (open) with angles relative to burner axial centerline

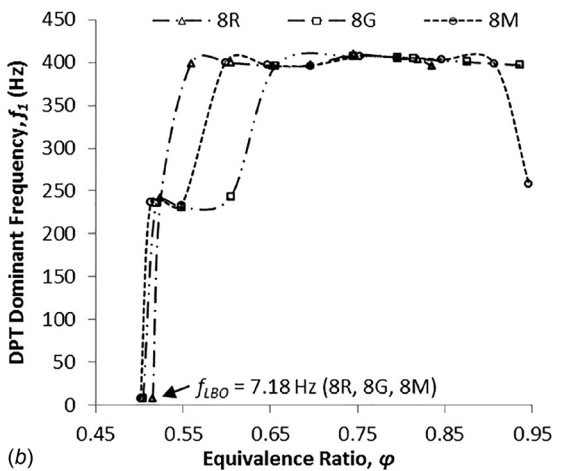
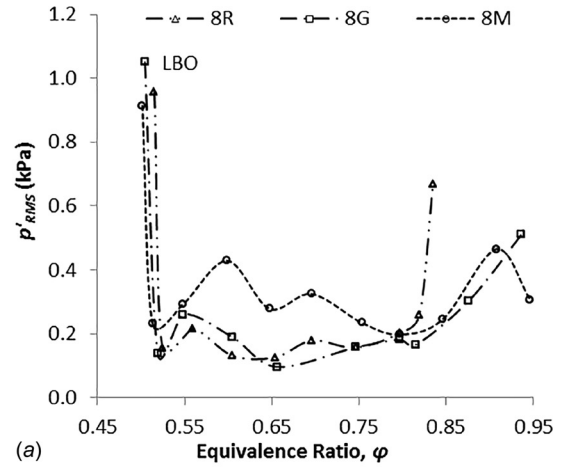


Fig. 10 Dynamic pressure (a) amplitude and (b) dominant frequency as a function of equivalence ratio for all swirlers

modulate the flame surface, imposing heat release fluctuations which are in phase with the dynamic pressure fluctuation, leading to a limit cycle instability. Of the three swirlers, the grit-blasted 8G swirler shows the widest stable operating range of all three swirlers, with p'_{RMS} below 0.4 kPa for the range $0.52 < \phi < 0.90$. This suggests a level of surface finish for ALM radial-tangential swirlers which could yield an advantage to stable operation across a wide range of flow conditions.

As mentioned previously, Fig. 11 provides insight into the dynamic behavior of each individual swirler, with 8R (Fig. 11(a)), 8G (Fig. 11(b)), and 8M (Fig. 11(c)). In Fig. 11, the frequencies of both the first (f_1 , open symbols) and second (f_2 , closed symbols) dominant dynamic pressure fluctuation modes are plotted against equivalence ratio along with the normalized amplitude of the second mode to the first mode (M_{f_2}/M_{f_1} , hashed symbols). Dashed lines are imposed for clarity only. It is expected when M_{f_1}/M_{f_2} is near unity that the system could be considered bimodal, and indeed conditions were identified where lean stability mode switching could occur (indicated in Fig. 11 by arrows). Bimodal stability was first identified in swirler 8G at $\phi=0.75$, where $M_{f_2}/M_{f_1}=0.89$. It is interesting to note that it is at this ϕ in Figs. 8 and 9, where the 8G and 8R swirler OH^* chemiluminescence intensity and centroid location are nearly identical, providing indication of the increasing influence of the bimodal stability on flame heat release with increasing reactivity. Figure 11(a) provides evidence of a mode switch from a ~ 250 Hz dominant frequency to ~ 400 Hz dominant frequency near $\phi=0.55$ in the 8R swirler with increasing ϕ . A similar mode switch shifts to higher equivalence ratio ($\phi \sim 0.64$) for the 8G swirler in Fig. 11(b). Both a

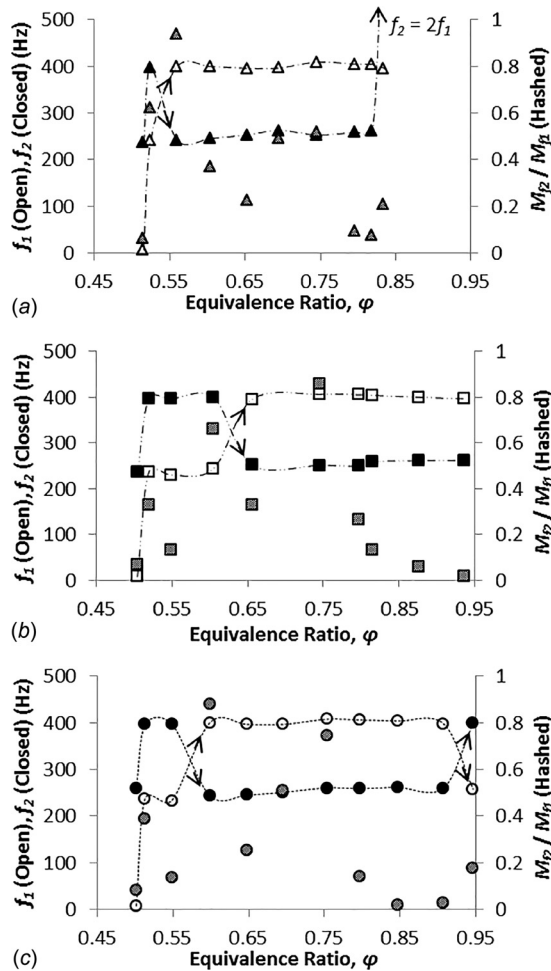


Fig. 11 First (open) and second (closed) mode frequencies and normalized amplitude (hashed) as a function of equivalence ratio for (a) 8R, (b) 8G, and (c) 8M

lean ($\phi \approx 0.57$) and near-stoichiometric ($\phi \approx 0.92$) mode switch were observed in the 8M swirler (Fig. 11(c)). This behavior was further confirmed by evaluation of the time-varying Π'_{OH^*} signal at conditions where $M_{f1}/M_{f2} \approx 1$.

Finally, it can be seen in Figs. 10 and 11 that all swirlers experience a similar LBO instability, with identical low frequency of $f_{LBO} = 7.18$ Hz (shown in Fig. 10(b)), confirmed by both dynamic pressure measurement and instantaneous OH^* chemiluminescence measurement. For example, in the 8R LBO case shown in Fig. 12, the phase difference between time-varying Π'_{OH^*} and p' signals was measured as 37 deg, satisfying the Rayleigh criterion for instability. Phase-averaged imaging in Fig. 12 of this low-frequency, high-amplitude instability from the 8R swirler at $\phi = 0.515$ is produced using 64 images for each phase, for a total

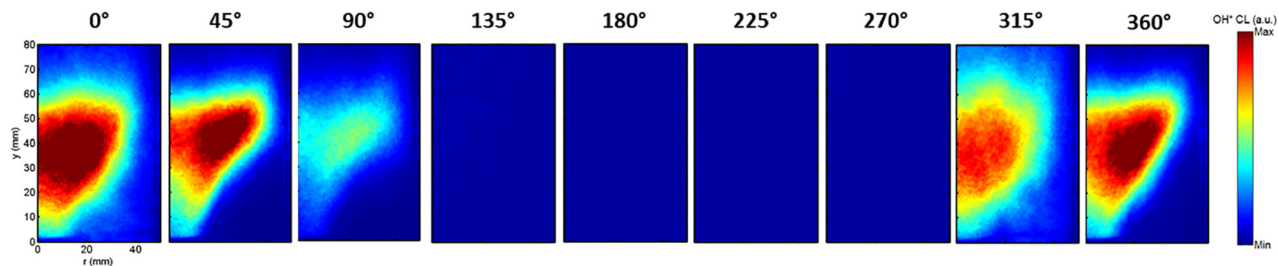


Fig. 12 Phase-averaged OH^* chemiluminescence images of LBO instability at $\phi = 0.515$ for the 8R swirler. Identical false colormap applied to all images.

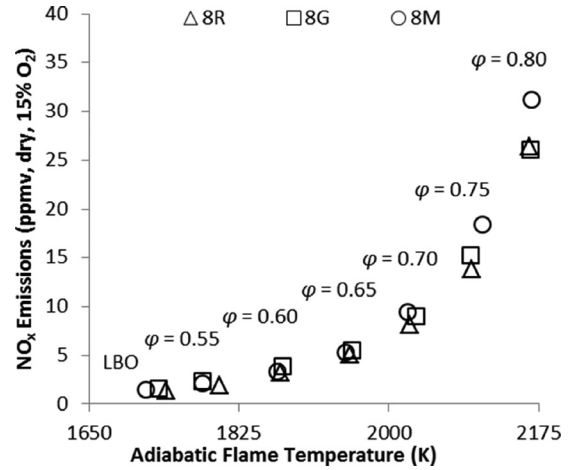


Fig. 13 NO_x emissions as a function of AFT and swirler surface roughness

time between images of $t = 0.016$ s. This instability is characterized by bulk flame extinction and reignition events, with flame detachment from the burner exit nozzle, downstream axial motion and reduction in heat release, and then reignition of the fresh incoming premixed fuel/air through the CRZ, and finally reattachment to the burner exit nozzle. A similar LBO instability was observed for the 8M swirler at ambient temperature conditions in Ref. [22]. The instability frequency appears to be independent of the swirler surface roughness; however, there is a slight lean shift in LBO equivalence ratio with decreased surface roughness. This suggests that the 8M swirl flame, with its stronger CRZ, is able to maintain stable combustion under highly turbulent conditions, as local temperatures in the flow field would be increased at the root of the flame, resulting in increased reactivity.

3.4 Exhaust Gas Emissions. Exhaust NO_x measurements were taken at each experimental condition with each swirler to identify any potential contribution or reduction from the change in surface roughness. NO_x production in these lean premixed flames is expected to be dominated by the thermal NO_x pathway [34]. However, given that swirler surface roughness has been shown to influence the flow field, turbulence intensity, and flame stabilization location, a measurable influence on NO_x emissions could be expected. By maintaining near identical volumetric flow through each swirler for a fixed equivalence ratio, AFT could be isolated as a contributing factor to thermal NO_x production. This can be observed in Fig. 13, which shows the expected exponential response in measured NO_x formation with increasing AFT (thus, increasing ϕ). NO_x emissions below 35 ppmv could be achieved across a wide range of AFT.

Within the measurement error of the gas analysis system, NO_x emissions at $AFT \leq 2000$ K are nominally similar for all swirlers, with sub-5 ppmv NO_x achievable under stable operating conditions. Above 2000 K, however, there is an observable offset

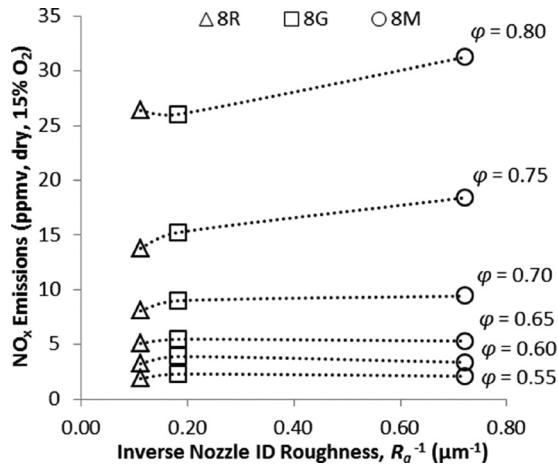


Fig. 14 NO_x emissions as a function of inverse swirler surface roughness

between the machined swirler, 8M, and the ALM swirlers, 8R and 8G. This behavior is more apparent in Fig. 14, which plots measured NO_x emissions against the inverse of a representative swirler surface roughness value taken as R_a of the swirler nozzle ID (surface roughness decreasing from left to right). Note that dotted lines are superimposed for clarity. Under lean conditions below $\phi = 0.65$, NO_x formation appears to be independent of the swirler surface roughness. Above $\phi = 0.65$, NO_x formation is seen to increase with decreasing surface roughness, with over 18% increase at $\phi = 0.80$.

4 Conclusions

Three generic gas turbine radial-tangential swirlers, 2 produced using ALM and the third produced by traditional machining methods, were investigated experimentally using high-speed diagnostics to characterize the influence of varying surface roughness on the resulting flow field, flame stability, and NO_x emissions. Stable operating regimes between a well-defined LBO instability and two rich stability limits were identified for a fixed thermal power of 25 kW by varying the air mass flow rate to adjust the exit velocity and equivalence ratio. This work aimed to provide a detailed characterization of the influence and potential benefits of surface features generated during ALM component fabrication, and to highlight the importance of considering these features during the design process and CFD modeling. The following distinct conclusions can be drawn from this work:

- (1) Radial-tangential gas turbine swirler geometry can be achieved using ALM with high-strength, high-temperature materials. Also, a 40% reduction in R_a of “raw” ALM components was achieved using a postbuild grit blast. The resulting R_a remains approximately twice that of a machined part.
- (2) The magnitude of isothermal positive and negative axial velocities is observed to decrease with increasing surface roughness while also shifting the shear layer toward the burner centerline. The maximum axial velocity gradient width is shown to increase up to 15% with increasing surface roughness, corresponding to an increase in turbulence.
- (3) Despite maintaining similar bulk axial velocities, OH^* chemiluminescence distribution was observed to shift upstream with reduced surface roughness. Mean OH^* chemiluminescence intensities were seen to increase with increasing surface roughness, indicative of enhanced heat release due to an increase in turbulence and therefore flame consumption speed near the burner exit.
- (4) All swirlers were observed to experience a similar LBO instability with a frequency of 7.18 Hz, characterized by

bulk extinction and re-ignition events. Transition to higher frequency modes is observed with increasing ϕ , with increasing surface roughness shown to dampen lean instabilities due to enhanced turbulence, but potentially promote rich instabilities due to increased heat release fluctuations.

- (5) The combustion system exhibits bimodal stability, with dominant frequencies of ~ 250 Hz and 400 Hz across all swirlers, with surface roughness shown to influence the operating condition at which the mode switching occurs. It is posited that high-turbulence fluctuations near the nozzle ID of swirler 8R contribute to the onset of a limit cycle instability near $\phi = 0.8$, which was not observed in the other swirlers.
- (6) Corrected NO_x emissions follow an expected thermal NO_x production trend with increasing AFT. At $\phi > 0.65$, increasing surface roughness was observed to reduce NO_x emissions for nominally similar AFT and exhaust gas temperature due to residence time effects.

Acknowledgment

This work was supported by funding from the Renishaw plc – Cardiff University Strategic Partnership Fund, the Advanced Gas Turbine project (UK Engineering and Physical Sciences Research Council Grant EP/M015300/1), and the FLEXIS project (Welsh European Funding Office Grant 80835). Nick Jones from Renishaw plc and Andrew Jones from HiETA Technologies are acknowledged for their input and facilitation of the ALM swirl burner construction and coordinate measurement. Dr. Alastair Clarke and William Britton are also acknowledged for their support in the surface roughness measurements. Finally, Jack Thomas and Terry Treherne are thankfully acknowledged for their work operating and maintaining the experimental facility. Information on the data underpinning the results presented here, including how to access them, can be found in the Cardiff University data catalogue at the website link.²

Funding Data

- Renishaw plc—Cardiff University Strategic Partnership Fund (Funder ID: 10.13039/100013208).
- The Advanced Gas Turbine project (UK Engineering and Physical Sciences Research Council Grant No. EP/M015300/1; Funder ID: 10.13039/501100000266).
- The FLEXIS project (Welsh European Funding Office Grant 80835).

Nomenclature

- AFT = adiabatic flame temperature
- ALM/AM = additive (layer) manufacturing
- CFD = computational fluid dynamics
- CRZ = central recirculation zone
- HPGSB-2 = high-pressure generic swirl burner (Mk. II)
- HPOC = high-pressure optical chamber
- LBO = lean blowoff
- LDA = laser Doppler anemometry
- SLM = selective laser melting
- 8G = grit-blasted ALM swirler, $S_g = 0.8$
- 8M = machined swirler, $S_g = 0.8$
- 8R = “raw” ALM swirler, $S_g = 0.8$

Symbols

- f_1 = burner dominant mode frequency (Hz)

²<http://doi.org/10.17035/d.2019.0079832309>

f_2 = burner secondary mode frequency (Hz)
 I'_{OH^*} = instantaneous integrated OH* intensity (a.u.)
 M_{f1} = burner dominant mode amplitude (kPa)
 M_{f2} = burner secondary mode amplitude (kPa)
 p'_{RMS} = RMS dynamic pressure amplitude (kPa)
 P_2 = burner inlet pressure (MPa)
 R_a = arithmetic average surface roughness (μm)
 R_q = RMS surface roughness (μm)
 R_z = ten-point mean surface roughness (μm)
 Re = Reynolds number
 S_g = geometric swirl number
 T_2 = burner inlet temperature (K)
 T_3 = burner outlet temperature (K)
 u = axial velocity component (m/s)
 \bar{u} = mean nozzle exit axial velocity (m/s)
 u'_{RMS} = RMS axial velocity fluctuation (m/s)
 y = axial direction (mm)
 ΔP = swirler pressure drop (kPa)
 ϕ = equivalence ratio

References

- [1] Frazier, W. E., 2014, "Metal Additive Manufacturing: A Review," *J. Mater. Eng. Perform.*, **23**(6), pp. 1917–1928.
- [2] Ford, S., and Despeisse, M., 2016, "Additive Manufacturing and Sustainability: An Exploratory Study of the Advantages and Challenges," *J. Cleaner Prod.*, **137**, pp. 1573–1587.
- [3] Attaran, M., 2017, "The Rise of 3-D Printing: The Advantages of Additive Manufacturing Over Traditional Manufacturing," *Bus. Horiz.*, **60**(5), pp. 677–688.
- [4] Gebisa, A. W., 2018, "Additive Manufacturing for the Manufacture of Gas Turbine Engine Components: Literature Review and Future Perspectives," *ASME Paper No. GT2018-76686*.
- [5] Appleyard, D., 2015, "Powering Up on Powder Technology," *Met. Powder Rep.*, **70**(6), pp. 285–289.
- [6] Sieger, M., 2017, "A New Dimension for Industry: How 3D Printing Is Doing Its Part to Reduce Greenhouse Emissions," General Electric, Boston, MA, *GE Reports*.
- [7] Navrotsky, V., Graichen, A., and Brodin, H., 2015, "Industrialisation of 3D Printing (Additive Manufacturing) for Gas Turbine Components Repair and Manufacturing," Siemens AG, Munich, Germany, accessed Oct. 11, 2018, <https://www.energy.siemens.com/hq/pool/hq/services/industrial-applications/additive-manufacturing/VGB-PowerTech-2015-12-NAVROTSKY-Autorexemplar.pdf>
- [8] Larfeldt, J., Andersson, M., Larsson, A., and Moëll, D., 2017, "Hydrogen Co-Firing in Siemens Low NOx Industrial Gas Turbines," POWER-GEN Europe, Cologne, Germany, June 27–29, pp. 1–12.
- [9] Ishizaka, K., Ito, E., Masada, J., Saitoh, K., and Yuri, M., 2017, "Key Technologies for 1700 °C Class Ultra High Temperature Gas Turbine," *Mitsubishi Heavy Ind. Tech. Rev.*, **54**(3), pp. 23–32.
- [10] Dryepontd, S., Kirka, M., Pint, B. A., and Daniel, R., 2016, "Comparison of Electron Beam and Laser Beam Power Bed Fusion Additive Manufacturing Process for High Temperature Turbine Component Materials," CRADA Final Report, Oak Ridge National Laboratory, Oak Ridge, TN, Report No. NFE-15-05495.
- [11] MAN Turbo & Diesel, 2017, "MAN Turbo & Diesel: 3D Printing Becomes a Standard," MAN Energy Solutions, Augsburg, Germany, accessed Oct. 11, 2018, <https://corporate.man-es.com/press-media/news-overview/details/2017/04/19/man-diesel-turbo-3d-printing-becomes-a-standard>
- [12] Capstone Turbine Corporation, 2018, "Capstone Unveils a New Product and Technology Development Roadmap—Including a C65 Signature Series Product, New Microgrid Products and Expanded Fuel Flexibility," Capstone Turbine Corporation, Van Nuys, CA, accessed Oct. 11, 2018, <https://www.capstoneturbine.com/news/press-releases/detail/3635/>
- [13] Andersson, O., Graichen, A., Brodin, H., and Navrotsky, V., 2017, "Developing Additive Manufacturing Technology for Burner Repair," *ASME J. Eng. Gas Turbines Power*, **139**(3), p. 031506.
- [14] Giuliani, F., Paulitsch, N., Cozzi, D., Görtler, M., and Andrachter, L., 2018, "An Assessment on the Benefits of Additive Manufacturing Regarding New Swirler Geometries for Gas Turbine Burners," *ASME Paper No. GT2018-75165*.
- [15] Mumtaz, K., and Hopkinson, N., 2010, "Selective Laser Melting of Thin Wall Parts Using Pulse Shaping," *J. Mater. Process. Technol.*, **210**(2), pp. 279–287.
- [16] Achenbach, E., and Heinecke, E., 1981, "On Vortex Shedding From Smooth and Rough Cylinders in the Range of Reynolds Numbers 6×10^3 to 5×10^6 ," *J. Fluid Mech.*, **109**, pp. 239–251.
- [17] Antonia, R. A., and Krogstad, P.-Å., 2001, "Turbulence Structure in Boundary Layers Over Different Types of Surface Roughness," *Fluid Dyn. Res.*, **28**(2), pp. 139–157.
- [18] Hossainpour, S., and Hakak Khadem, M., 2010, "Investigation of Fluid Flow and Heat Transfer Characteristics of Gases in Microchannels With Consideration of Different Roughness Shapes at Slip Flow Regime," *Nanoscale Microscale Thermophys. Eng.*, **14**(3), pp. 137–151.
- [19] Maeda, S., Masashi, F., Ienaga, S., Hirahara, K., and Obara, T., 2019, "Effect of Sandpaper-Like Small Wall Roughness on Deflagration-to-Detonation Transition in a Hydrogen-Oxygen Mixture," *Proc. Combust. Inst.*, **37**(3), pp. 3609–3616.
- [20] Al-Fahham, M., Hatem, F. A., Alsaegh, A. S., Valera-Medina, A., Bigot, S., and Marsh, R., 2017, "Experimental Study to Enhance Flashback Resistance for Boundary Layer Flashback in Swirl Burners Using Microsurfaces," *ASME Paper No. GT2017-63367*.
- [21] Pritz, B., Magagnato, F., and Gabi, M., 2008, "Investigation of the Effect of Surface Roughness on the Pulsating Flow in Combustion Chambers With LES," EU-Korea Conference on Science and Technology (EKC), Heidelberg, Germany, Aug. 28–31, pp. 69–76.
- [22] Runyon, J., Marsh, R., Bowen, P., Pugh, D., Giles, A., and Morris, S., 2018, "Lean Methane Flame Stability in a Premixed Generic Swirl Burner: Isothermal Flow and Atmospheric Combustion Characterization," *Exp. Therm. Fluid Sci.*, **92**, pp. 125–140.
- [23] Pugh, D., Bowen, P., Valera-Medina, A., Giles, A., Runyon, J., and Marsh, R., 2019, "Influence of Steam Addition and Elevated Ambient Conditions on NO_x Reduction in a Staged Premixed Swirling NH₃/H₂ Flame," *Proc. Combust. Inst.*, **37**(4), pp. 5401–5409.
- [24] Pugh, D., Bowen, P., Crayford, A., Marsh, R., Runyon, J., Morris, S., and Giles, A., 2018, "Catalytic Influence of Water Vapor on Lean Blow-Off and NO_x Reduction for Pressurized Swirling Syngas Flames," *ASME J. Eng. Gas Turbines Power*, **140**(6), p. 061502.
- [25] Bons, J. P., 2010, "A Review of Surface Roughness Effects in Gas Turbines," *ASME J. Turbomach.*, **132**(2), p. 021004.
- [26] Runyon, J., Marsh, R., Pugh, D., Bowen, P., Giles, A., Morris, S., and Valera-Medina, A., 2017, "Experimental Analysis of Confinement and Swirl Effects on Premixed CH₄-H₂ Flame Behavior in a Pressurized Generic Swirl Burner," *ASME Paper No. GT2017-64794*.
- [27] ANSYS, 2017, "ANSYS Chemkin-Pro 19.0," ANSYS, Canonsburg, PA.
- [28] Smith, G. P., Golden, D. M., Frenklach, M., Moriarty, N. W., Eiteneer, B., Goldenberg, M., Bowman, C. T., Hanson, R. K., Song, S., Gardiner, W. C., Jr., Lissianski, V. V., and Qin, Z., 1999, "The 'GRIMEch 3.0' Chemical Kinetic Mechanism," accessed Oct. 1, 2019, www.me.berkeley.edu/grimech
- [29] Hook, S., Clarke, A., and Evans, H. P., 2018, "Generation of Acoustic Emission From the Running-in and Subsequent Micropitting of a Mixed-Elastohydrodynamic Contact," *Tribol. Int.*, **119**, pp. 270–280.
- [30] Strano, G., Hao, L., Everson, R., and Evans, K. E., 2013, "Surface Roughness Analysis, Modelling and Prediction in Selective Laser Melting," *J. Mater. Process. Technol.*, **213**(4), pp. 589–597.
- [31] Lieneke, T., Denzer, V., Adam, G., and Zimmer, D., 2016, "Dimensional Tolerances for Additive Manufacturing: Experimental Investigation for Fused Deposition Modeling," *Procedia CIRP*, **43**, pp. 286–291.
- [32] Shepherd, I. G., and Cheng, R. K., 2001, "The Burning Rate of Premixed Flames in Moderate and Intense Turbulence," *Combust. Flame*, **127**(3), pp. 2066–2075.
- [33] Han, Z., and Hochgreb, S., 2015, "The Response of Stratified Swirling Flames to Acoustic Forcing: Experiments and Comparison to Model," *Proc. Combust. Inst.*, **35**(3), pp. 3309–3315.
- [34] Prade, B., 2013, "Gas Turbine Operation and Combustion Performance Issues," *Modern Gas Turbine Systems: High Efficiency, Low Emission, Fuel Flexible Power Generation*, Woodhead Publishing, Cambridge, UK, pp. 383–422.